Metal-phenolic-network-coated gold nanoclusters for enhanced photothermal/chemodynamic/immunogenic cancer therapy

Tingyu Yang [a],[1], Liqun Dai [a],[1], Jie Liu [a], Yi Lu [a], Meng Pan [a], Lili Pan [b], Lin Ye [c], Liping Yuan [a], Xicheng Li [a], Zhongwu Bei [a], Zhiyong Qian [a],[*]

[a] Department of Biotherapy, Cancer Center and State Key Laboratory of Biotherapy, West China Hospital, Sichuan University, Chengdu, 610041, China
[b] Department of Nuclear Medicine and Clinical Nuclear Medicine Research Lab, West China Hospital, Sichuan University, Chengdu, Sichuan, 610041, China
[c] Department of Ophthalmology, West China Hospital, Sichuan University, Chengdu, Sichuan, 610041, China

ARTICLE INFO

ABSTRACT

Triple-negative breast cancer (TNBC) is the most aggressive subtype of breast cancer, characterised by a short survival period, high malignancy, strong invasiveness, and high rates of recurrence and metastasis. Due to its unique molecular phenotype, TNBC is insensitive to endocrine therapy or molecular targeted therapy. The conventional treatment approach involves systemic chemotherapy for overall management; however, adjuvant chemotherapy after surgery has shown poor efficacy as residual lesions can easily lead to tumour recurrence. Therefore, there is an urgent need to find more effective treatment strategies. Herein, we designed a gold nanocluster coated with a metal-phenol formaldehyde network structure (AuNCs@PDA-Mn) for tumour Photothermal therapy and chemodynamic therapy (PTT and CDT), which induces systemic immune responses to suppress tumour metastasis. Experimental results show that after continuous irradiation for 10 min under an 808 nm laser ($1.0 W/cm^2$), AuNCs@PDA-Mn not only exhibits better tumour inhibition both in vitro and in vivo but also triggers stronger immune effects systemically. Therefore, this combined PTT and CDT treatment approach has great potential and provides a clinically relevant and valuable option for triple-negative breast cancer.

1. Introduction

Breast cancer poses a significant concern due to its high incidence and mortality rates, rendering it the most prevalent malignant ailment afflicting women [1]. In recent years, a progressive increase in the incidence of breast cancer has been observed in numerous developing countries, coinciding with a rising trend of earlier disease onset among affected individuals [2]. Molecular classification criteria permit the categorisation of breast cancer as follows: Luminal A, Luminal B, HER-2 overexpression, and triple-negative breast cancer (TNBC) [3]. Of these subtypes, TNBC is distinguished by its aggressive nature, with a reduced survival time, elevated degree of malignancy, heightened invasiveness, and increased risks of recurrence and metastasis [4]. Due to its unique molecular phenotype, TNBC is insensitive to endocrine therapy or molecular targeted therapy [5]. The conventional treatment approach involves systemic chemotherapy for overall management; however, adjuvant chemotherapy after surgery has shown poor efficacy as residual lesions can easily lead to tumour recurrence [6]. It is therefore imperative that more effective treatment strategies are identified [7,8].

In recent years, photothermal therapy (PTT) has emerged as a promising alternative to conventional treatments due to its relatively gentle nature [9]. PTT has demonstrated significant potential in the ablation of solid tumours by utilising near-infrared laser (NIR) irradiation locally or interstitially through optical fibres [10]. Simultaneously, the integration of photothermal therapy with immunotherapy and chemotherapy has yielded significant advances in cancer treatment [11–13]. Intracellular thermal therapy has been demonstrated to stimulate the release of tumour antigens and pro-inflammatory cytokines, encompassing heat shock proteins (HSPs), adenosine triphosphate (ATP), and high mobility group box 1 protein (HMGB1) [14–16]. The

---

process of immunogenic cell death allows for the exposure of relevant antigens from deceased cells, which can subsequently potentiate antigen-specific T cell responses [17,18]. Furthermore, released damage-associated molecular patterns (DAMPs) act as "danger" signals for immune stimulation, augmenting dendritic cell phagocytosis of tumour antigens, facilitating dendritic cell maturation, triggering the activation of cytotoxic CD8+ T cells and helper CD4+ T cells, thereby initiating anti-tumour immunity to synergistically eradicate cancerous cells [19–21]. In photothermal therapy, gold nanoparticles exhibit the capacity to efficiently absorb incident light and convert it into thermal energy, thereby effectively destroying tumour cells [22]. Gold nanoclusters (AuNCs), consisting of several to hundreds of gold atoms, are a class of ultra-small inorganic nanoparticles with well-defined chemical composition and atomic structure. In addition, they have a relatively stable multi-core aggregate structure, small size, good water solubility, and biocompatibility [23,24]. AuNCs are therefore widely used in biological imaging [25], disease diagnosis [26], and cancer therapy [27]. There are two main methods for synthesising gold nanoclusters, bottom-up and top-down, but both involve tedious steps [26,28,29].

Chemokinetic therapy (CDT) effectively induces the production of hydroxyl radicals (·OH) through the Fenton reaction, leading to cancer cell death in an oxygen-independent manner [30,31]. Due to the limited catalytic efficiency and the presence of H_2O_2 in cells, the single treatment of CDT has a limited effect, which hinders its further application. To achieve thermal effects, it becomes crucial to expedite the Fenton reaction process to induce the generation of hydroxyl radicals, thereby accomplishing synergistic outcomes of combined cancer photothermal therapy and chemotherapy (CDT/PTT) [32–36]. Mn^{2+}, as a Fenton reagent, can convert endogenous hydrogen peroxide to free radicals in the presence of bicarbonate in the tumour microenvironment. This conversion can effectively deplete GSH and enhance the efficacy of CDT; therefore, Mn^{2+} has been widely used in tumour therapy [37–39]. For instance, Wu and coworkers recently reported a high-performance near-infrared II (NIR-II) fluorescence imaging-guided molecular photo theranostic platform (IR-FE-Fc@DSPE-S-S-PEG) with good biocompatibility and enhanced Fenton reaction efficiency, which could reverse immunosuppression and stimulated the immune system in a mouse model [40]. More recently, Li and coworkers prepared a tumour microenvironment (TME) specifically responsive POM@MOF composites with sequential activation properties for synergistic PTT/CDT treatment, which releases PMo_{12} and Fe^{3+} under acidic TME conditions and are subsequently converted into reduced PMo_{12} and Fe^{2+} by GSH in the TME to achieve excellent photothermal conversion efficiency and accelerated the disproportionation efficiency of H_2O_2 for enhancing the synergistic CDT/PTT and cancer ablation [41]. However, multifunctional nanomedicine typically necessitates intricate preparation procedures, which significantly impedes their antitumour applications. Consequently, in cancer therapy, the creation of a multifunctional nanomaterial with glutathione depletion, tumour targeting, and PTT/CDT synergy for effective anti-tumour therapy through straightforward methods represents a crucial yet challenging endeavour.

Dopamine (DA) can serve as a structure-guiding agent for the selective deposition of gold atoms on specific crystal planes, leading to the formation of nanoparticles with anisotropic structures [42]. The remarkable adsorption capability of PDA enables its firm attachment onto the surface of AuNCs, resulting in the formation of specifically polydopamine-coated gold nanoclusters (AuNCs@PDA) under stirring conditions, thereby conferring appropriate biocompatibility and stability upon the nanoparticles [43]. Furthermore, PDA exhibits chelation properties towards various metal ions for constructing metal-phenolic networks; additionally, its surface modification can be employed as a "bridge" for efficient Mn^{2+} collection on nanoparticles [44].

In this study, our objective is to employ PDA for reducing HAuCl4 to prepare AuNCs and constructing a metal-phenolic network encapsulating gold nanoclusters (AuNCs@PDA-Mn) that can be utilised in heat treatment and chemical dynamics therapy combined with antitumour

effects. The AuNCs@PDA-Mn nanoparticles are designed to penetrate the tumour via the EPR effect and exploit the acidic pH environment within the tumour for controlled release of Mn^{2+}. Upon laser irradiation, these gold nanoclusters generate thermal energy to effectively eradicate tumour cells while also accelerating the Fenton reaction process to stimulate hydroxyl radical production, thereby achieving a synergistic CDT/PTT effect that further inhibits tumour growth and metastasis.

2. Materials and methods

2.1. Materials and animals

HAuCl4 (99.99 % trace metals basis, 30 wt % in dilute HCl) was purchased from Sigma-Aldrich (Saint Louis, USA). Dopamine hydrochloride ($C_8H_{11}NO_2$·HCl, DA, ≥98 %) was purchased from Aladdin Reagent (Shanghai, China); Na_2HPO_4、NaH_2PO_4、NaOH and H_3PO_4 were purchased from Chron Chemicals (Chengdu, China). (7S,8S)-7-(2-Carboxyethyl)-5-(carboxymethyl)-18-ethyl-2,8,12,17-tetramethyl-13-vinyl-7H,8H-porphyrin-3-carboxylic acid was purchased from Bidepharm (Shanghai, China). 2′,7′-dichlorofluorescin diacetate (H2DCFDA), and fetal bovine serum (FBS) were purchased from Yeason (Shanghai, China). Annexin V-FITC/PI Apoptosis Detection Kit、Lyso-Tracker Green, and HCS DNA Damage Kit were purchased from Beyotime (Shanghai, China). Dulbecco's modified Eagle's medium (DMEM) and Phosphate buffered saline (PBS) were purchased from Gibco (USA). TMRM perchlorate was purchased from MedChemExpress (Shanghai, China). Rabbit anti-HMGB1 Polyclonal Antibody was purchased from Absin (Shanghai, China). Calreticulin (D3E6) XP Rabbit mAb was purchased from Cell Signaling Technology; Mouse IL-6 ELISA Kit, mouse TNF-α ELISA Kit, mouse IFN-γ ELISA Kit, mouse IFN-β ELISA Kit, mouse IL-10 ELISA Kit, mouse IL-12p70 ELISA Kit were purchased from Neo-Bioscience (Shenzhen, China). PE Hamster Anti-Mouse CD80, BV421 Rat Anti-Mouse TNF, APC Rat Anti-Mouse IFN-γ, APC Hamster Anti-Mouse CD49b, APC-Cy7 Rat Anti-Mouse CD45, APC Hamster Anti-Mouse CD11c, PE-Cy7 Rat Anti-Mouse CD86, FITC Hamster Anti-Mouse CD3e, PE Rat Anti-Mouse CD4, PerCP-Cy5.5 Rat Anti-Mouse CD8a were purchased from BD Pharmingen (USA).

BALB/c mice (6 weeks old) were obtained from the Gempharmatech Company (China) and kept under a specific-pathogen-free condition with free access to standard food and water. All animal experiments were performed following the protocols approved by the Ethics Committee of the Animal Experimental Center of State Key Laboratory of Biotherapy of Sichuan University (Checking number: 20210409028).

2.2. Preparation and characterisation of AuNCs@PDA and AuNCs@PDA-Mn

2.2.1. Preparation of AuNCs@PDA-Mn nanoparticles

Firstly, the AuNCs@PDA-Mn was synthesised according to the previously reported method with some modifications. In Dopamine hydrochloride (20 mg) was added to phosphate buffer solution (pH = 8.5) at room temperature. The mixture was vigorously stirred for 5 min. Then auric chloride (10 μL) was added to the mixture for 10 min. During this period of time the colour of the solution changed from light yellow to dark brown quickly. The AuNCs@PDA solution was collected by centrifugation for 10 min (8000r/min) and washed 3 times with MilliQ water. The precipitate was redispersed into 8 mL water. Then $MnCl_2$ (5 mg) was mixed with the redispersed solution and vigorously stirred overnight at room temperature. Subsequently, the products were collected by centrifugation (8000 rpm) for 10 min and washed with excess water.

2.2.2. Characterisation

The morphologies and composition of AuNCs@PDA and AuNCs@PDA-Mn were determined by transmission electron microscope (TEM; Talos F200S) equipped with an energy-dispersive x-ray

spectroscopy (EDS) system. The particle size distribution and zeta potentials were determined by dynamic light scattering (Malvern Zetasizer Nano ZSP system ZEN5600), respectively. The concentration of manganese and gold elements was characterised by iCAP Q inductively coupled plasma mass spectrometry (ICP-MS). The X-ray photoelectron spectroscopy (XPS) spectra were measured by ThermoFischer ESCALAB 250Xi. UV–vis spectra were obtained using a SHIMADZU UV-2600 UV–vis spectrophotometer. XRD was measured by Rigaku Ultima IV X-ray diffractogram.

2.2.3. Detection of ·OH

Firstly, AuNCs@PDA-Mn and AuNCs@PDA were dispersed in water (final concentration = 25, 50, 100, 200, 400 µg/mL), well mixed with an H_2O_2 solution (final concentration = 10 mM) and an MB solution (final concentration = 10 µg/mL) and incubated at room temperature for 3 h. The ·OH-induced MB degradation was quantified by UV–vis spectroscopy at 665 nm. For comparison, the blank MB solution and H_2O_2/MB mixture solution were also tested under the same conditions.

2.2.4. NIR-II luminescence

Downshifting luminescence emission spectra of AuNCs@PDA-Mn were recorded under 808 nm excitation and captured by an infrared thermal camera. After administrated with AuNCs@PDA-Mn and AuNCs@PDA solutions, NIR-II images of orthotopic 4T1-bearing mice were obtained under 808 nm excitation.

2.3. Cellular experiments

2.3.1. Cellular uptake

4T1 cells were seeded in 6-well plates at a density of 2×10^5 cells per well with 1.0 mL of medium and incubated at 37 °C in 5 % CO_2 overnight. Then, 50 µg/mL AuNCs@PDA-Mn-Ce6 and AuNCs@PDA-Ce6 with fresh medium were added and further incubated for 4h. After treating with AuNCs@PDA-Mn-Ce6 and AuNCs@ PDA-Ce6, the cells were stained with Lysotracker Green, Mitotracker Green and ER-tracker Green. After washing with PBS, the cells were stained with Hoechst and washed with PBS three times. Finally, the fluorescence imaging was performed by laser confocal microscopy.

2.3.2. CCK-8 assay

4T1 cells were seeded in 96-well plates at a density of 8000 cells per well with 100 µL of medium and incubated at 37 °C in 5 % CO_2 overnight. Then, the medium was replaced with fresh medium containing AuNCs@PDA-Mn and AuNCs@PDA at different concentrations (25, 50, 100, 200, 400 µg/mL, respectively) and incubated for 4h. The cells were then washed with PBS three times and cultured with fresh medium. The cells of the NIR group were irradiated under the 808 nm laser at a power density of 1.0 W/cm^2 for 5 min, respectively, and then were subsequently cultured for 24h. After that, the cells were then incubated with 100 µL fresh medium with 10 % CCK-8. After a 1h co-incubation, the optical density value was measured at 450 nm using a microplate reader. The relative cell viability was acquired by calculating the percentage of viable cells in total cells.

2.3.3. Intracellular ROS generation

4T1 cells were seeded in confocal at a density of 2×10^5 cells per well with 1.0 mL of medium and incubated at 37 °C in 5 % CO_2 overnight. After attachment, 100 µg/mL AuNCs@PDA-Mn and AuNCs@PDA were added and incubated for 4h. The cells were then washed with PBS three times and incubated in PBS containing 10 µM H2DCFDA in the dark for 30 min. Afterwards, the cells of the NIR group were irradiated under the 808 nm laser at a power density of 1.0 W/cm^2 for 5 min respectively. Finally, cells were observed by confocal fluorescence microscopy. Untreated tumour cells were used as control.

2.3.4. Intracellular GSH detection

4T1 cells were seeded in confocal at a density of 2×10^5 cells per well with 1.0 mL of medium and incubated at 37 °C in 5 % CO_2 overnight. After attachment, 100 µg/mL AuNCs@PDA-Mn and AuNCs@PDA were added and incubated for 4h. Afterwards, the cells of the NIR group were irradiated under the 808 nm laser at a power density of 1.0 W/cm^2 for 5 min respectively. The cells were then incubated in PBS containing 10 µM GSH tracker in the dark for 30 min. Finally, cells were observed by confocal fluorescence microscopy. Untreated tumour cells were used as control.

2.3.5. Intracellular LPO detection

4T1 cells were seeded in confocal at a density of 2×10^5 cells per well with 1.0 mL of medium and incubated at 37 °C in 5 % CO_2 overnight. After attachment, 100 µg/mL AuNCs@PDA-Mn and AuNCs@PDA were added and incubated for 4h. Afterwards, the cells of the NIR group were irradiated under the 808 nm laser at a power density of 1.0 W/cm^2 for 5 min respectively. Then, the cells were treated by a C11-BODIPY581/591 probe for 20min in the dark and washed with PBS for three times. Finally, cells were stained with Hoechst and observed by confocal fluorescence microscopy.

2.3.6. γ-H2AX staining for DNA fragments

4T1 cells were seeded in confocal at a density of 2×10^5 cells per well with 1.0 mL of medium and incubated at 37 °C in 5 % CO_2 overnight. After attachment, 100 µg/mL AuNCs@PDA-Mn and AuNCs@PDA were added and incubated for 4h. Afterwards, the cells of the NIR group were irradiated under the 808 nm laser at a power density of 1.0 W/cm^2 for 5 min respectively. Then, the cells were treated with an HCS DNA Damage Kit. Finally, cells were stained with Hoechst and observed by confocal fluorescence microscopy.

2.3.7. TRMR assay

4T1 cells were seeded in confocal at a density of 2×10^5 cells per well with 1.0 mL of medium and incubated at 37 °C in 5 % CO_2 overnight. After attachment, 100 µg/mL AuNCs@PDA-Mn and AuNCs@PDA were added and incubated for 4h. Afterwards, the cells of the NIR group were irradiated under the 808 nm laser at a power density of 1.0 W/cm^2 for 5 min respectively. Then, the cells were carefully washed with PBS and dyed with JC-1 and were observed by confocal fluorescence microscopy.

2.3.8. Apoptosis/necrosis evaluation

4T1 cells were seeded in confocal at a density of 2×10^5 cells per well with 1.0 mL of medium and incubated at 37 °C in 5 % CO_2 overnight. After attachment, 100 µg/mL AuNCs@PDA-Mn and AuNCs@PDA were added and incubated for 4h. Afterwards, the cells of the NIR group were irradiated under the 808 nm laser at a power density of 1.0 W/cm^2 for 5 min respectively. Then, the cells were carefully washed with PBS and stained with annexin-V FITC and propidium iodide (PI) according to the manufacturer's protocol and observed by confocal fluorescence microscopy.

2.3.9. Immunogenic cell death (ICD) effect

4T1 cells were seeded in confocal at a density of 2×10^5 cells per well with 1.0 mL of medium and incubated at 37 °C in 5 % CO_2 overnight. After attachment, 100 µg/mL AuNCs@PDA-Mn and AuNCs@PDA were added and incubated for 4h. Afterwards, the cells of the NIR group were irradiated under the 808 nm laser at a power density of 1.0 W/cm^2 for 5 min respectively. After incubation for 10h, the cells were washed with PBS and stained by anti-CRT antibody for 30 min. Then, the cells were washed and observed by confocal fluorescence microscopy. To detect the HMGB1 and ATP, the cells were treated with nanoparticles as the detection of CRT expression experiment method. After being irradiated under the 808 nm laser at a power density of 1.0 W/cm^2 for 5 min and incubated for another 10h, the cell culture medium was collected and used for the detection of HMGB1 and ATP. The HMGB1 evaluation was

conducted by an Elisa assay. The ATP detection was conducted by an ATP detection kit according to the manufacturer's instructions.

2.4. In vivo anti-tumour effect and immune response assay

2.4.1. In vivo fluorescence imaging

4T1 tumour-bearing mice were iv. injected with PBS, AuNCs@PDA-Mn-Ce6 and AuNCs @PDA-Ce6 (1 mg/mL, 200 μL). In vivo imaging system Lumina XR was used to scan the whole body at different time points (1h, 4h, 8h, 12h, and 24h). Major organs were collected and scanned at 8 h and 24 h, respectively. The mean fluorescence intensity of tumours and major organs was collected for the semi-quantitative data analysis.

2.4.2. In vivo anti-tumour activity assay

Female Balb/c mice (6–8 weeks old) were orthotopically inoculated with 4T1 cells in the fore limb. A suspension of 5×10^6 4T1 tumour cells in PBS solution was implanted into the right fore limb, designated as the primary tumour, and 1×10^6 tumour cells into the contralateral limb, designated as the distant tumour. When primary tumour sizes reached ~100 mm^3, the tumour-bearing mice were randomised into six groups (n = 5 per group) and administered with PBS, AuNCs@PDA-Mn and AuNCs @PDA (1 mg/mL, 200 μL) by tail-vein injection, respectively. 4 h later, the mice of the NIR group were irradiated under the 808 nm laser at a power density of 1.0 W/cm^2 for 10 min respectively. These treatments were repeated four times every other day for 7 days, and the tumour volume and body weight of each mouse were monitored every other day for 14 days, and the tumour volume was calculated according to the formula of Volume = Width^2 × Length/2.

2.4.3. In vivo ROS detection

4T1 tumour-bearing mice were i.v. injected with PBS, AuNCs@PDA-Mn and AuNCs @PDA (1 mg/mL, 200 μL). After 4h, the mice were intratumorally injected with DCFH-DA (50 μL, 1.0 mg/mL). The mice of the NIR group were irradiated under the 808 nm laser at a power density of 1.0 W/cm^2 for 10 min respectively. The fluorescent signal of the tumour was detected by an in vivo fluorescence imaging system. Then, the mice were sacrificed, and the tumour was collected for ex vivo fluorescence imaging. After that, the tumour was frozen for DHE staining.

2.4.4. Flow cytometric analysis and cytokine detection

After treatment, the mice were sacrificed, and lymph nodes and spleens were isolated and filtered through cell strainers to obtain single-cell suspensions, respectively. Then, the cells were isolated and homogenised in the suspension based on a reported protocol. After that, cells were counted and stained with different panels of antibodies according to the vendor's protocols. For the T cells, cells were stained with FITC Hamster Anti-Mouse CD3e, PE Rat Anti-Mouse CD4, PerCP-Cy5.5 Rat Anti-Mouse CD8a, BV421 Rat Anti-Mouse TNF and APC Rat Anti-Mouse IFN-γ. For activated DCs analysis, APC-Cy7 Rat Anti-Mouse CD45, APC Hamster Anti-Mouse CD11c, PE-Cy7 Rat Anti-Mouse CD86 and PE Hamster Anti-Mouse CD80 were used. To analyse NK cells, APC Hamster Anti-Mouse CD49b, APC-Cy7 Rat Anti-Mouse CD45 and FITC Hamster Anti-Mouse CD3e were used.

Cytokines in the serum and tumour tissue homogenate were measured by ELISA kits according to the protocols, including IL-6, TNF-α, IL-12p70, IFN-γ, IFN-β, and CXCL10.

2.4.5. Histological and biosafety examinations

At 14 days post-treatment, the mice were sacrificed, and tumours, lymph nodes and major organs (heart, lung, spleen, liver and kidney) were collected in paraformaldehyde for hematoxylin and eosin staining. Meanwhile, the tumour tissues were sectioned into slices for TdT-mediated dUTP Nick-End Labeling (TUNEL) and Ki67 staining, and the lymph nodes were sectioned into slices for CD11c staining.

To further confirm the biosafety of the AuNCs@PDA-Mn and AuNCs @PDA complexes, the healthy mice were divided into three groups (n = 3) and intravenously administrated with 200 μL of PBS, AuNCs@PDA-Mn and AuNCs @PDA (1 mg/mL). At 7 days post-injection, the mice were sacrificed, and the blood was collected and stabilised with heparin for blood routine and blood biochemical analysis. The tested biochemical items included alanine aminotransferase (ALT), glutamic oxalacetic transaminase (AST), alkaline phosphatase (ALP), creatinine (CR), uric acid (UA), creatine kinase (CK), creatine kinase isoenzyme (CKMB), creatinine (CR), lactate dehydrogenase (LDH). The routine blood indices included white blood cell (WBC), red blood cell (RBC), mean corpuscular volume (MCV), mean corpuscular haemoglobin (MCH), lymphocyte (Lym), monocytes (Mon), and neutrophil (Neu).

2.5. Statistical analysis

All experimental data were represented as the mean ± standard deviation through at least three experiments. All statistical analyses were performed with GraphPad Prism 7.00 software. A P-value less than 0.05 was considered statistically significant (*P $<$ 0.05, **P $<$ 0.01, ***P $<$ 0.001, ****P $<$ 0.0001).

3. Results and discussion

3.1. Synthesis and characteristics of AuNCs@PDA and AuNCs@PDA-Mn

Under mild conditions, DA molecules can serve as stabilisers and reducing agents for the synthesis of gold nanoclusters (AuNCs). A homogeneous black colloidal solution of AuNCs can be obtained by mixing DA molecules with HAuCl$_4$ in a phosphate-buffered solution (PBS, pH 8.5), followed by stirring at room temperature for 10 min (Scheme 1). The loading efficiency of Mn^{2+} of AuNCs@PDA-Mn is 1.05 %, and the contents of Au in AuNCs@PDA and AuNCs@PDA-Mn are 51.43 % and 44.15 %, respectively (Table S1). As illustrated in the TEM images (Fig. 1a and S2), their average diameters of AuNCs@PDA and AuNCs@PDA-Mn were 51.48 ± 7.27 nm and 56.77 ± 5.46 nm. In the energy-dispersive X-ray spectroscopy (EDS) elemental map, signals of carbon (C), nitrogen (N), oxygen (O), gold (Au) and manganese (Mn) elements were further observed (Fig. 1b and S2). The average hydrodynamic diameter of AuNCs@PDA-Mn was determined to be approximately 302 nm (PDI = 0.1284) using dynamic light scattering (DLS) technology (Fig. 1e). The presence of a hydration layer leads to a substantial increase in nanoparticle size, and this increase in size is positively correlated with the contribution of dynamic light scattering (DLS) signals. High-resolution TEM (HR-TEM) images were applied to further reveal the features of this heterostructure. As can be observed, the lattice fringes of 0.225 nm corresponded to the d-spacing of the (111) plane of Au (Fig. 1c). Meanwhile, the selected area electron diffraction (SAED) pattern manifested the polycrystalline feature (Fig. 1a). This was consistent with the result from X-ray powder diffraction (XRD) (Fig. 1d).

Fourier transform infrared (FTIR) spectra were recorded to verify the formation of AuNCs@PDA and AuNCs@PDA-Mn (Fig. S3). The peaks at 1640 and 1566 cm^{-1} in both AuNCs@PDA and AuNCs@PDA-Mn correspond to the amide bonds formed between the carboxyl groups of DA and the other DA terminal amines. The peaks from 3255 to 3820 cm^{-1} in both AuNCs@PDA and AuNCs@PDA-Mn correspond to the hydroxyl group (-OH) and amino group (-NH$_2$) of PDA. After MPN encapsulation, the zeta potential is reduced from −12.3 mV for AuNCs@PDA to −24.13 mV for AuNCs@PDA-Mn (Fig. 1c). XPS spectra of the as-prepared AuNCs@PDA-Mn nanocomposites identified the coexistence of Au, Mn, C, N, and O and their chemical states in the final samples, illustrating the successful decoration of the AuNCs@PDA-Mn (Fig. 1g). Furthermore, the Au 4f spectrum exhibited two peaks at 83.7 and 87.3 eV, corresponding to metallic Au 4f$_{7/2}$ and Au 4f$_{5/2}$ bands, respectively (Fig. 1h). Additionally, the Mn 2p spectrum indicated that the majority of this element is present in the Mn^{2+} form (Fig. 1i).
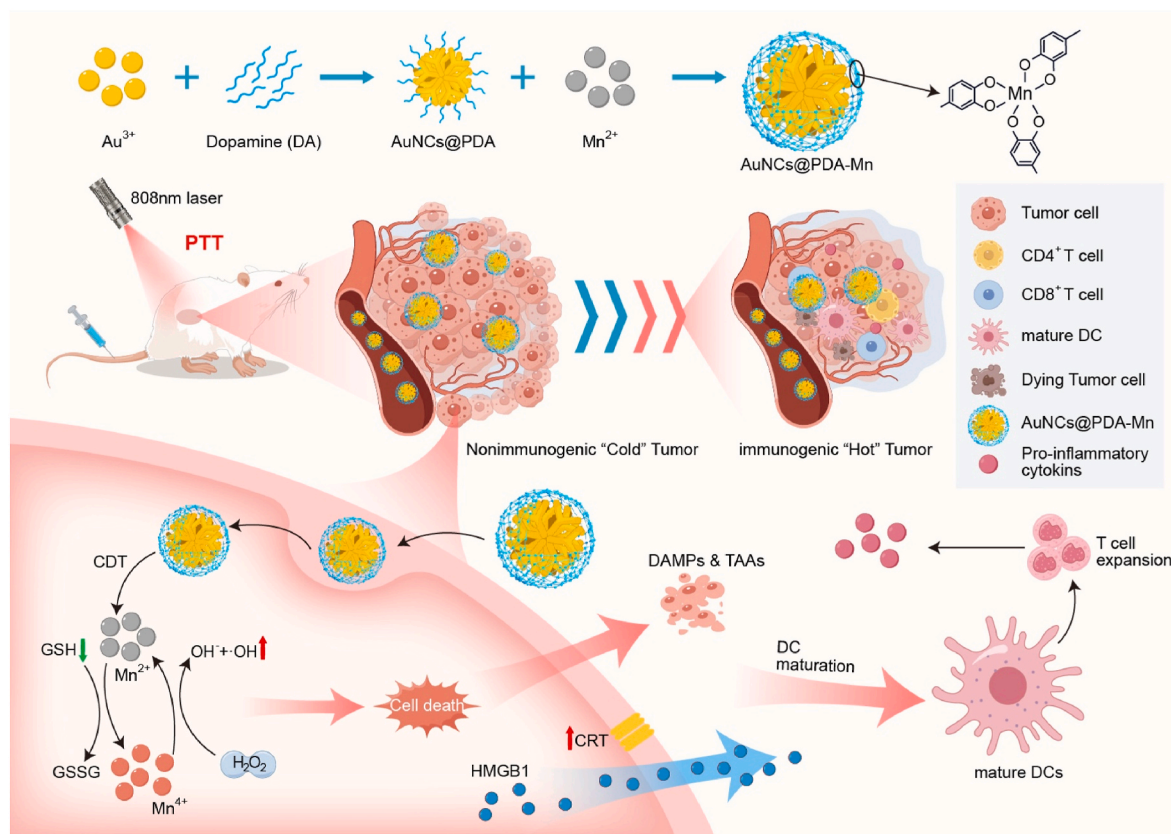
Scheme 1. Schematic illustration of the preparation of AuNCs@PDA-Mn for PTT and CDT of tumours and activating immunogenic effect systematically.

The subsequent evaluation of the catalytic Fenton-like reaction ability of AuNCs@PDA and AuNCs@PDA-Mn was conducted utilising a quantitative detection of the generation of reactive oxygen species (ROS) utilising methylene blue (MB) as an indicator. The colouration of the methylene blue (MB) solution gradually dissipates as the hydroxyl radicals (·OH) degrade the dye. The AuNCs@PDA and AuNCs@PDA-Mn solutions with varying concentrations were co-incubated with 10 mM H_2O_2 and 10 μg/mL MB at 37 °C for 30 min. In this study, H_2O_2 was employed to simulate the tumour microenvironment, while MB served as an indicator to assess the generation of ·OH. As depicted in Fig. S4, upon co-culturing with AuNCs@PDA, a significant reduction in absorption at 665 nm was observed for MB, indicating the degradation of MB by AuNCs@PDA. Additionally, with the increase in PDA concentration, the degradation amount of MB gradually escalates, whereas in the control group, the absorbance value of MB remains consistently stable. This phenomenon can be attributed to PDA serving as an electron donor receptor for GSH and subsequently transferring electrons to MB, which acts as the final electron acceptor after phenol is reduced to quinone. Furthermore, upon incubation with MB and H_2O_2, AuNCs@PDA-Mn exhibited a significant reduction in absorbance within the 550–700 nm range compared to AuNCs@PDA. This phenomenon can be attributed to the Mn^{2+}-induced Fenton-like reaction, which results in the generation of reactive oxygen species and subsequent fading of MB. These findings highlight the potential of both AuNCs@PDA and AuNCs@PDA-Mn for initiating chemodynamic activity against cancer cells.

3.2. Photothermal property studies

The photothermal performance of the as-prepared AuNCs@PDA and AuNCs@PDA-Mn were investigated. AuNCs@PDA and AuNCs@PDA-Mn exhibited excellent optical absorption characteristics and stability within the near-infrared window, indicating their potential to convert near-infrared energy into heat for raising solution temperature. The clear UV–visible absorption spectra shown in Fig. 2 and Fig. S5 confirmed the promising application prospects of AuNCs@PDA (Fig. S5a) and AuNCs@PDA-Mn (Fig. 2g and h) as a photothermal agent in the biomedical field. Additionally, the temperature of the dispersed solution rose gradually with increasing concentrations of AuNCs@PDA (Fig. S5c) and AuNCs@PDA-Mn (Fig. 2a and b). The infrared thermal images of AuNCs@PDA-Mn with different concentrations were recorded over a 10-min irradiation period, as illustrated in Fig. 2a. Following a 10-min irradiation period, the temperature of AuNCs@PDA and AuNCs@PDA-Mn at a concentration of 400 μg/mL increased by 19.2 °C and 24.8 °C respectively, whereas the corresponding DI water only rose by 4.7 °C and 4.9 °C. Furthermore, Fig. 2c illustrates that the photothermal conversion efficiency of AuNCs@PDA-Mn is linearly proportional to the laser power density and increases with increasing laser power density. The photothermal conversion efficiency (PTCE) is a crucial metric for evaluating the therapeutic efficacy of photothermal agents. In the wavelength of 808 nm, with a power density of 1.0 W/cm², the temperature of 200 μg/mL AuNCs@PDA-Mn could rise by 17.5 °C when subjected to continuous radiation (Fig. 2d) while AuNCs@PDA rose 16 °C under the same conditions (Fig. S5d). Subsequently, the photothermal cycling performance of AuNCs@PDA-Mn was evaluated by performing five consecutive heating and cooling cycles with 10 min each of radiation and 10 min of off-radiation at 808 nm, 1.0 W/cm². The experimental results demonstrated that after five consecutive cycles, AuNCs@PDA-Mn continued to exhibit excellent dispersion ability concerning temperature rise, thereby confirming that it exhibited excellent thermal stability (Fig. 2e). The photothermal conversion efficiency (η) of AuNCs@PDA and AuNCs@PDA-Mn was calculated to be 54.23 % (Figure. S5b, d and e) and 65.6 % (Fig. 2d–g and h) based on the cooling fitting curve. These findings indicated that AuNCs@PDA and AuNCs@PDA-Mn may be appropriate for mild photothermal therapy (PTT) targeting cancer cells.
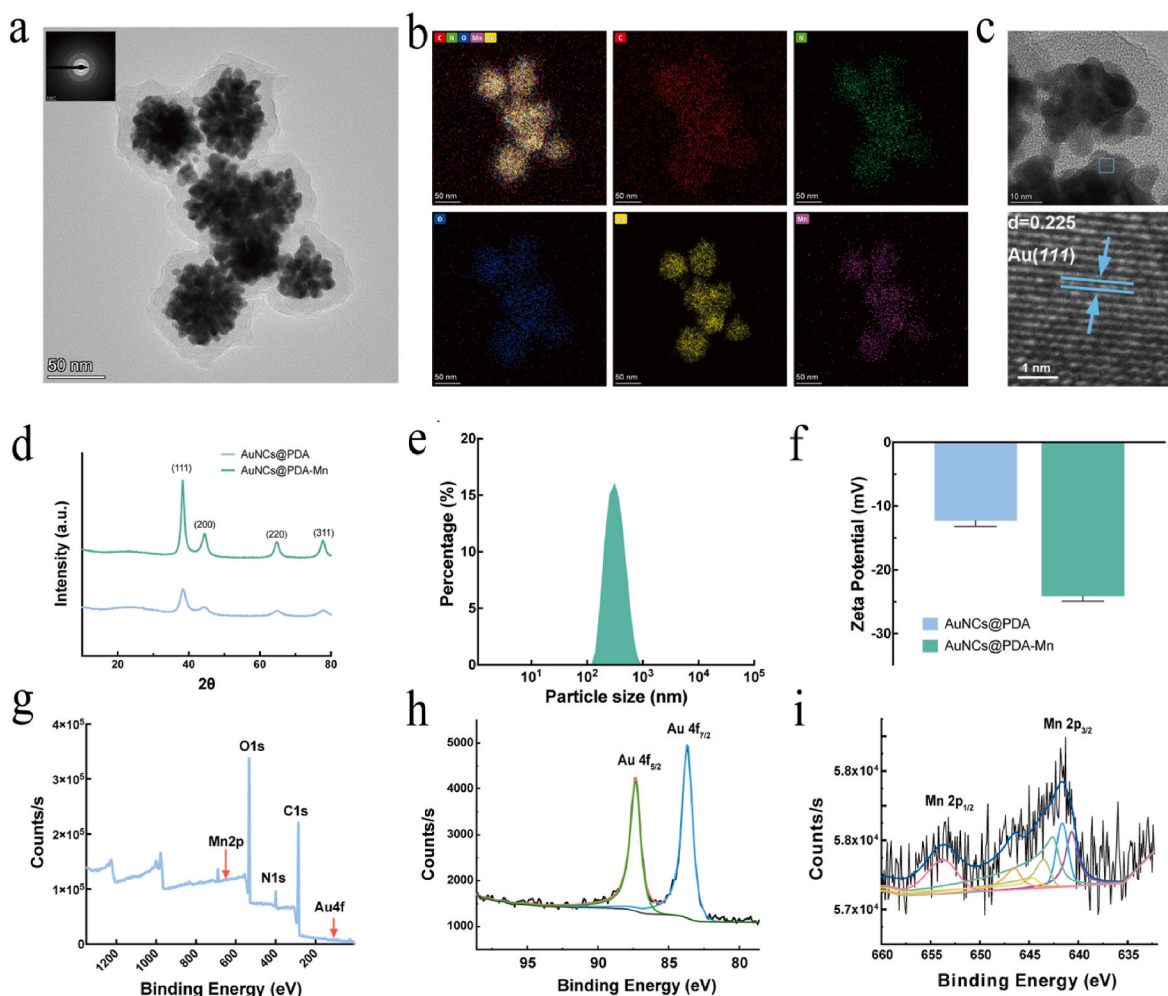
Fig. 1. Characterisation of AuNCs@PDA and AuNCs@PDA-Mn. a) TEM image (Insert: SAED pattern) (Scale bar: 100 nm). b) elemental mappings (Scale bar: 50 nm) of AuNCs@PDA-Mn. c) HR-TEM images. d) The XRD pattern of AuNCs@PDA and AuNCs@PDA-Mn. e) Dynamic light scattering analysis (DLS) of the hydrodynamic size distribution of AuNCs@PDA-Mn. f) Comparisons of the zeta potentials of AuNCs@PDA and AuNCs@PDA-Mn in water. g) X-ray photoelectron spectroscopy (XPS) analysis data of AuNCs@PDA-Mn. h) Au 4f electronic energy spectra of AuNCs@PDA-Mn. i) Mn2p electronic energy spectra of AuNCs@PDA-Mn. Data are presented as mean ± SD (n = 3).

3.3. In vitro cancer cells-killing capability

The endocytic pathways of AuNCs@PDA-Mn were investigated utilising fluorescent markers of different organelles. Confocal laser scanning microscopy (CLSM) was used to validate the in vitro cellular internalisation of AuNCs@PDA-Mn, which was achieved through the labelling of the nanoparticles with Chlorin e6 (Ce6). The higher fluorescence overlapped between lysosomes and Ce6-loaded AuNCs@PDA-Mn than between mitochondria and the endoplasmic reticulum suggested that lysosome-mediated endocytosis was assisted by mitochondrial- and ER-mediated endocytic pathways (Fig. 3b and Fig. S6). Following incubation periods of 0, 1, 2 and 4 h, the observed Ce6-loaded AuNCs@PDA-Mn red fluorescence in the cytoplasm exhibited a gradual enhancement (Fig. 3c). This indicated that the cells exhibited a positive correlation between the absorption of AuNCs@PDA-Mn and the incubation time.

In vitro cell counting kit-8 (CCK-8) assays were performed to evaluate the impact of various treatments on cell viability. 4T1 cells were incubated with AuNCs@PDA and AuNCs@PDA-Mn at varying concentrations (0–400 μg/mL) for a period of 4h. Subsequently, the 808 nm laser was employed, with a density of 1.0 W/cm² for a 5 min exposure. Following irradiation, incubation was continued for 20 h under suitable conditions. As illustrated in Fig. 3a, the cytotoxic effect of irradiation

increased with increasing concentrations of AuNCs@PDA and AuNCs@PDA-Mn, resulting in a gradual decline in 4T1 cell viability. The results demonstrated that photothermal treatment was significantly efficacious against cancer cells at high concentrations of AuNCs@PDA and AuNCs@PDA-Mn. Furthermore, laser irradiation augmented the cytotoxicity of AuNCs@PDA and AuNCs@PDA-Mn. This augmented effect may be attributed to the toxic ROS substances produced. In addition, live and dead cell co-staining was employed to evaluate the impact of different treatment regimens on cellular viability. Specifically, Calcein-AM (green) and propidium iodide (red) were utilised for cell labelling in order to discriminate between viable and non-viable cells. As illustrated in Fig. 3e, the PBS group exhibited green fluorescence, with no red fluorescence observed, indicating that the cells were all in a viable state. Following processing, a small quantity of red fluorescence was observed in the AuNCs@PDA-Mn group, indicating that a limited number of cells had initiated the apoptotic process. However, following incubation with AuNCs@PDA and AuNCs@PDA-Mn, the addition of an 808 nm laser at a power of 1.0 W/cm² for 5 min resulted in the observation of intense red fluorescence, indicating that all cells were dead. The results demonstrated a correlation between the early stages of cell apoptosis and mitochondrial membrane dysfunction. Therefore, the TMRM dye was employed to assess the impact of AuNCs@PDA + L and AuNCs@PDA-Mn + L on mitochondrial function. The fluorescence
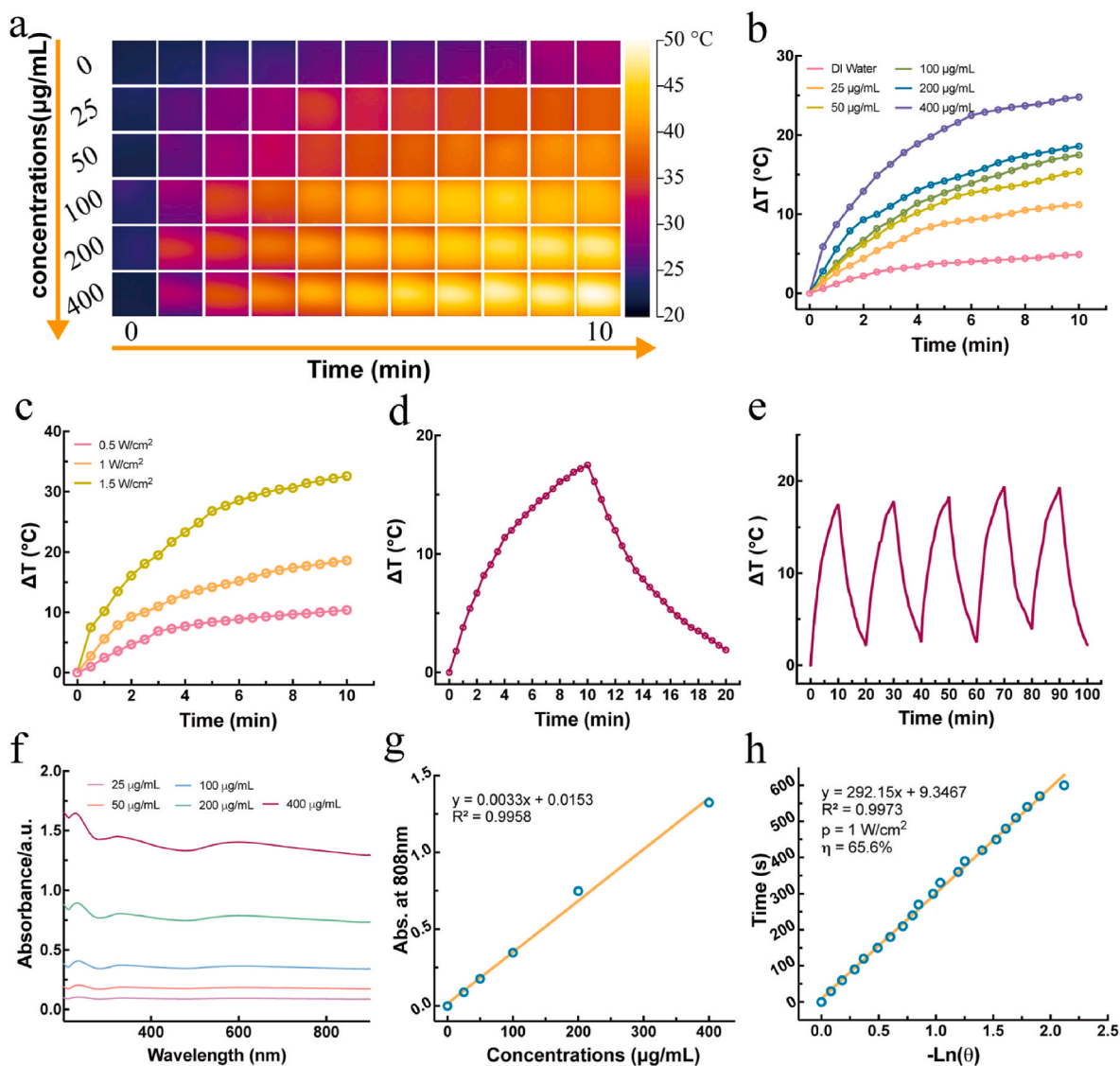
Fig. 2. In vitro photothermal-conversion performance. a) Infrared pictures and b) photothermal heating curves of different concentrations of AuNCs@PDA-Mn solution after irradiation (808 nm, 1.0W/cm^2, 10min). c) Photothermal-heating curves of AuNCs@PDA-Mn solution (200 µg/mL) after irradiation at varied power densities (0.5 W/cm^2, 1.0 W/cm^2, 1.5 W/cm^2). d) Photothermal-heating and cooling curves of AuNCs@PDA-Mn solution (200 µg/mL) after irradiation (808 nm, 1.0W/cm^2, 10min). e) Photothermal profiles of the suspension of AuNCs@PDA-Mn solution (200 µg/mL) over five irradiation cycles. f) UV–vis spectra of AuNCs@PDA-Mn solutions with elevated concentrations. g) The absorbance of AuNCs@PDA-Mn solutions with elevated concentrations at 808 nm. h) Linear time data versus −Ln(θ).

observed in normal mitochondria was red, gradually fading as the mitochondrial membrane potential decreased. As illustrated in Fig. S7a, the fluorescence intensity of 4T1 cells treated with AuNCs@PDA + L and AuNCs@PDA-Mn + L was found to be significantly lower than that of PBS controls, indicating that mitochondrial function was severely impaired. This finding further confirms the effectiveness of PTT in inducing cell death. Furthermore, flow cytometry was employed to assess the efficacy of the indicated treatments in killing 4T1 cancer cells. The results indicated that the ratio of dead/apoptotic cells in cell samples incubated with AuNCs@PDA-Mn + L was significantly higher than that observed in the other groups, which was consistent with the cytotoxic results (Fig. 3d).

To investigate the intracellular PTT effect, AuNCs@PDA and AuNCs@PDA-Mn were incubated with 4T1 cells for 4h, followed by a ROS probe H2DCFDA incubation for another 30 min. Subsequently, the cells were irradiated with an 808 nm laser for 5 min (1.0 W/cm^2) to observe the effects of PTT on the cells. The probe can be oxidised to form high-launch 7-hydroxy-3h-dichloro fluorescein (DCF), as shown in

Fig. 3f. Cells treated only with AuNCs@PDA and AuNCs@PDA-Mn showed weak green fluorescence in CLSM images compared to the PBS group. However, when compared to the irradiation group, the AuNCs@PDA + L and AuNCs@PDA-Mn + L groups exhibited significantly enhanced green fluorescence in the CLSM images. The results of the flow cytometry analysis were in accordance with the aforementioned findings (Fig. S8). This indicates that PTT had induced the ROS. These findings indicated that, in the presence of an 808 nm laser, AuNCs@PDA and AuNCs@PDA-Mn were successfully internalised, leading to the generation of ROS. Furthermore, the generation of ROS can be enhanced by increased oxidative stress, which can in turn lead to DNA damage in cells. Consequently, the probe γ-H2AX was employed to ascertain the extent of DNA double-strand breakage in cells subjected to ROS-induced injury. Following treatment with the various formulations, the fluorescence of γ-H2AX was barely discernible in the PBS, AuNCs@PDA and AuNCs@PDA-Mn groups. However, the AuNCs@PDA + L and AuNCs@PDA-Mn + L groups exhibited distinct green immunofluorescence, indicating that ROS could induce DNA breaks, which in
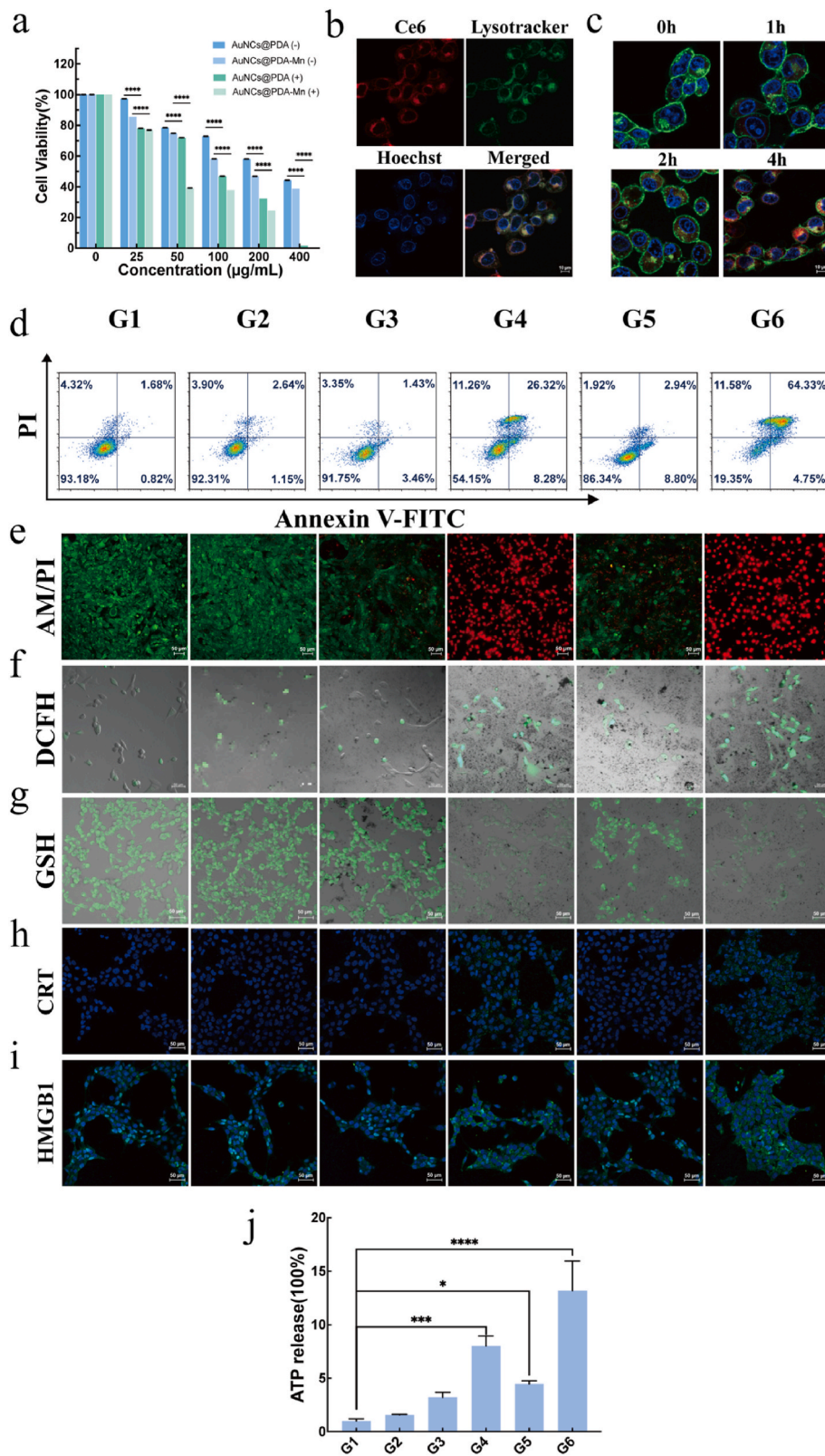
Fig. 3. a) Relative cell viability of 4T1 cells after incubation with different concentrations of AuNCs@PDA and AuNCs@PDA-Mn in the absence or presence of light irradiation (1.0 W/cm², 5 min). Data are presented as mean ± SD (n = 3). b) CLSM images of 4T1 cells incubated with AuNCs@PDA-Mn for 4 h. Blue fluorescence shows nuclear from Hoechst; red fluorescence is attributed to Ce6 labelled AuNCs@PDA-Mn; green fluorescence shows lysosomes from Lysotracker Green (Lyso Green). Scale bar: 10 μm. c) CLSM images of the cellular uptake of AuNCs@PDA-Mn at different times. Scale bar: 10 μm. d) The apoptosis and necrosis analysis of 4T1 cells after different treatments. e) Fluorescent morphology images of 4T1 cells exposed to various treatments after live and dead staining. Green fluorescence indicates the live cells and red fluorescence indicates dead cells. Scale bar: 50 μm. f) CLSM images of 4T1 cells stained with DCFH after different treatments. Green fluorescence indicates the ROS level. Scale bar: 50 μm. g) CLSM images of 4T1 cells stained with GSH tracker after different treatments. Green fluorescence indicates the GSH level. Scale bar: 50 μm. h) CRT expression after different treatments. Scale bar: 50 μm. i) HMGB1 release after different treatments. Scale bar: 50 μm. j) The any other group ratio of extracellular ATP concentration to the control group. G1: PBS; G2: PBS + L; G3: AuNCs@PDA; G4: AuNCs@PDA + L; G5: AuNCs@PDA-Mn; G6: AuNCs@PDA-Mn + L, in which the symbols "L", indicated the presence of NIR irradiation. Data are presented as mean ± SD (n = 3). Statistical significance was calculated via one-way ANOVA with Tukey's test: *p < 0.05; **p < 0.01; ***p < 0.001; ****p < 0.0001.

turn caused apoptosis (Fig. S7b).

To confirm the capacity of AuNCs@PDA and AuNCs@PDA-Mn to deplete glutathione (GSH), a GSH tracker was employed to assess intracellular GSH levels. In comparison to the PBS group, AuNCs@PDA following the processing of 4T1 cells demonstrated no significant reduction in green fluorescence, indicating that intracellular GSH levels were not significantly lower (Fig. 3g). The AuNCs@PDA-Mn can be driven by Mn^{2+} in a Fenton-like reaction, which results in the consumption of GSH and the subsequent increase in ROS levels. Consequently, the green fluorescence observed in the AuNCs@PDA-Mn cells is likely due to the aforementioned processes. CLSM images demonstrated that the green fluorescence of the AuNCs@PDA + L and AuNCs@PDA-Mn + L groups was markedly diminished, indicating that the GSH content was significantly lower than that of the control group. This indicates a synergistic effect of laser irradiation on intracellular GSH consumption, which is consistent with the results of increased intracellular ROS levels. The depletion of GSH in AuNCs@PDA + L and AuNCs@PDA-Mn + L may be attributed to the inhibition of glutathione peroxidase 4 (GPX-4) expression, which prevents the conversion of lipid peroxidation (LPO) into fatty alcohol. Subsequently, we utilised C11-BODIPY581/591 as a probe to determine the level of LPO in intracellular accumulation in 4T1 cells following different treatments via CLSM imaging. As the level of LPO in cells increases, the fluorescent signal undergoes a change from red to green. As illustrated in Fig. S7c, the green fluorescence was strongest, and the red fluorescence was weakest in cells treated with AuNCs@PDA + L and AuNCs@PDA-Mn + L compared with any other groups. This indicates that AuNCs@PDA + L and AuNCs@PDA-Mn + L were capable of producing a considerable amount of LPO, which may have contributed to the promotion of apoptosis.

In order to ascertain the efficacy of the combination therapy in activating the immune system, the impact of the 4T1 cells following different treatments on the induction of immune cell death (ICD) was evaluated. To verify the ICD effect of the cells, we examined the surface-exposed calreticulin (ecto-CRT) level, high mobility group protein b1 (HMGB1) and adenosine triphosphate (ATP) release of 4T1 cells under different treatments. These metrics are commonly employed to assess the degree of immunogenicity produced following cell death. Following laser irradiation, the 4T1 cells in the AuNCs@PDA + L and AuNCs@PDA-Mn + L treatment groups exhibited significantly elevated green fluorescence signals, indicative of higher ecto-CRT levels, in comparison to the cells treated solely with AuNCs@PDA and AuNCs@PDA-Mn (Fig. 3h). Furthermore, a reduction in fluorescence within the nucleus and an increase in fluorescence within the cytoplasm were observed in the AuNCs@PDA + L and AuNCs@PDA-Mn + L treatment groups, indicating that HMGB1 was released from the nucleus (Fig. 3i). In addition, the levels of ATP release were significantly increased after the AuNCs@PDA + L and AuNCs@PDA-Mn + L treatments, which were consistent with the results of CRT expression and HMGB1 release (Fig. 3j and S9). Notably, higher levels of CRT, HMGB1, and ATP were observed in the AuNCs@PDA + L and AuNCs@PDA-Mn + L groups, providing reliable evidence for the efficacy of PTT in triggering the ICD pathway. The combined therapy demonstrated a significant effect on ICD efficacy, as evidenced by CLSM and ATP release data.

3.4. In vivo distribution and ROS generation

Following a comprehensive hemolysis test, it was determined that AuNCs@PDA-Mn demonstrated excellent in vivo safety during intravenous administration. Fig. S10 illustrates that even after incubation for various time intervals, the tested concentration range of AuNCs@PDA-Mn did not induce significant hemolytic reactions. Notably, even at a concentration as high as 400 μg/mL, the observed hemolysis rate remains below 5 %, which is within the safe range required for in vivo studies.

A prerequisite for the accumulation of therapeutic agents in tumour sites is the prolongation of blood circulation time. The biodistribution characteristics of AuNCs@PDA-Mn were investigated by administering them into BALB/c mice bearing 4T1 tumours. As illustrated in Fig. S11a, the Ce6-loaded AuNCs@PDA-Mn exhibited a time-dependent accumulation pattern in tumours, with the strongest fluorescence observed at 4h post-injection, indicating the excellent tumour-targeting ability of AuNCs@PDA-Mn. The results of ICP-MS demonstrated a time-dependent accumulation of Au and Mn in the tumour, with a peak concentration at 4h post-administration (Figs. S11b and c). This further supports the hypothesis that these nanoparticles accumulate in tumours. The biodistribution results suggest that laser irradiation should be conducted 4h post-injection.

To investigate the in vivo PTT effect, we pre-injected the ROS probe H2DCFDA into the mouse tumour 30min before treatment administration. In comparison to the control groups, the AuNCs@PDA + L and AuNCs@PDA-Mn + L groups exhibited a discernible increase in fluorescence, indicating that PTT had triggered the generation of ROS (Fig. S11d). Following the removal of the tumour tissues, they were stained using the DHE probe. Upon examination of the same treatment time, a notable red fluorescence was observed when irradiation was present (Fig. S11e). The findings demonstrate that irradiation is a crucial factor in the generation of ROS at tumour sites.

3.5. Inhibition of established tumours and tumour metastasis

In light of the encouraging outcomes observed in vitro, we recently investigated the potential of AuNCs@PDA and AuNCs@PDA-Mn in combined photothermal therapy (PTT) and chemodynamic therapy (CDT) applications for tumour treatment in vivo. To validate the inhibitory effects of AuNCs@PDA and AuNCs@PDA-Mn on tumours in vivo, two different 4T1 orthotopic tumour models were established, comprising varying cell densities. The tumours were designated as primary tumours (on the right side) and distant tumours (on the left side). The tumour-bearing mice were randomly divided into 6 groups and intravenously injected with PBS, AuNCs@PDA, or AuNCs@PDA-Mn dispersion 4 times at specified time points. Subsequently, after 4h, half of the mice with primary tumours received 10 min of 808 nm laser treatment (1.0 W/cm²) (Fig. 4a). To confirm the in vivo photothermal effect, temperature measurements of the tumour sites were recorded every 30s under irradiation from an 808 nm laser for mice injected with PBS, AuNCs@PDA, or AuNCs@PDA-Mn dispersions and the infrared images were taken every minute. As illustrated in Fig. 4b and c, mice that had been injected with either AuNCs@PDA or AuNCs@PDA-Mn
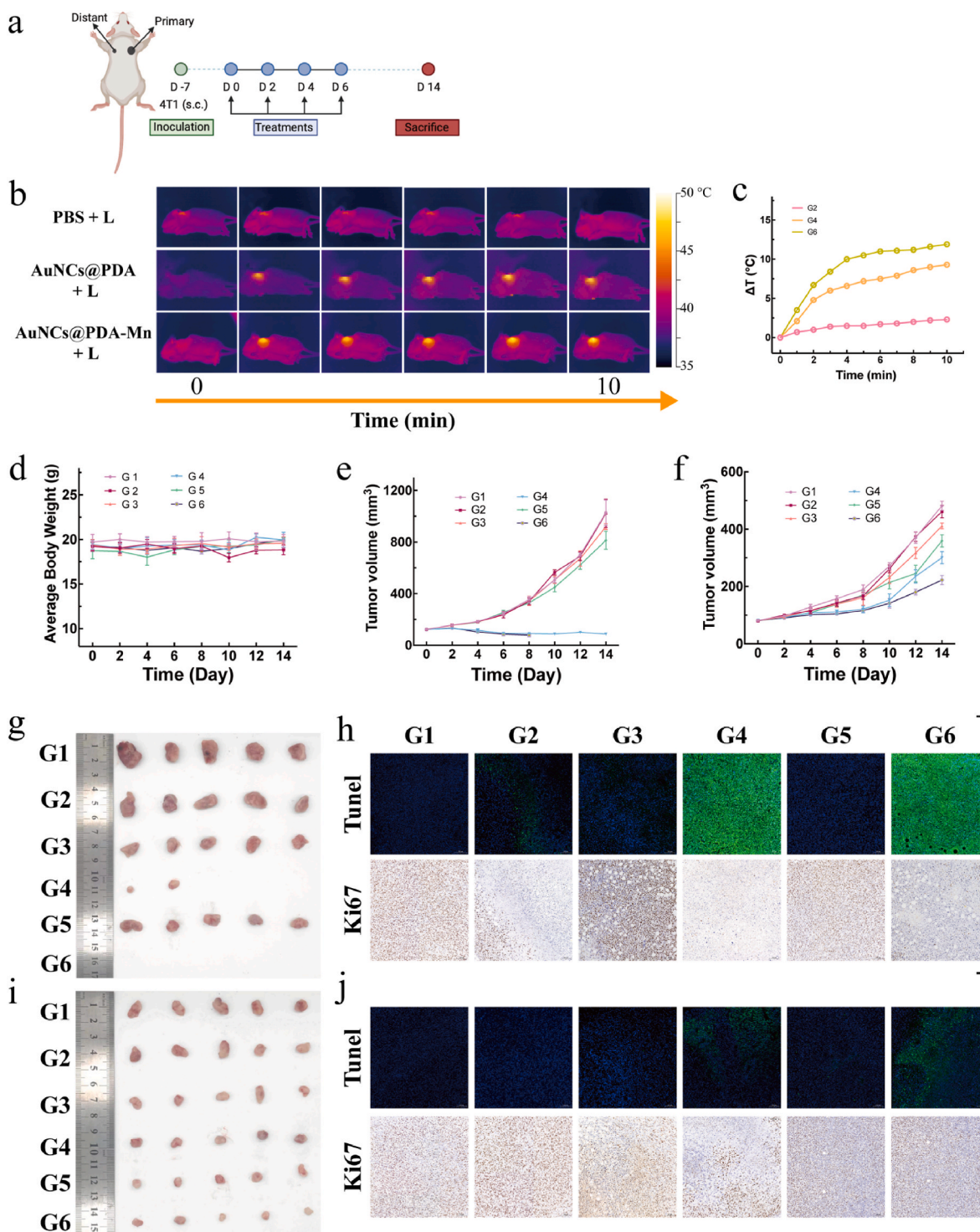
Fig. 4. a) Schematic illustration to evaluate the therapeutic efficacy and abscopal effect after treating with different formulations. b) Photothermal images of 4T1 tumour-bearing BALB/c mice after different treatments. c) The temperature increasing curves of the tumours. d) Corresponding body weights of mice in each group after the mice are treated for 14 days. e) Primary tumour growth curves. f) Distant tumour growth curves. g) Photographs of primary tumours. h) Tunnel and Ki67 staining of the primary tumour. Scale bar: 100 μm. i) Photographs of distant tumours. j) Tunnel and Ki67 staining of distant tumour. Scale bar: 100 μm. Data are presented as mean ± SD (n = 5). G1: PBS; G2: PBS + L; G3: AuNCs@PDA; G4: AuNCs@PDA + L; G5: AuNCs@PDA-Mn; G6: AuNCs@PDA-Mn + L, in which the symbols "L", indicated the presence of NIR irradiation.

exhibited a rapid increase in tumour temperature upon laser irradiation. Mice that had been injected with AuNCs@PDA-Mn demonstrated a slightly higher temperature elevation compared to those that had been injected with AuNCs@PDA alone. Within a span of 10 min, mice injected with AuNCs@PDA-Mn demonstrated an approximate temperature rise

of approximately 11.9 °C, while those injected with AuNCs@PDA only showed a temperature rise of approximately 9.3 °C. In contrast, the group receiving PBS injections had a maximum temperature rise of only approximately 2.3 °C. It can therefore be concluded that both AuNcs@PDA and AuNCs@PDA-Mn are capable of generating significant
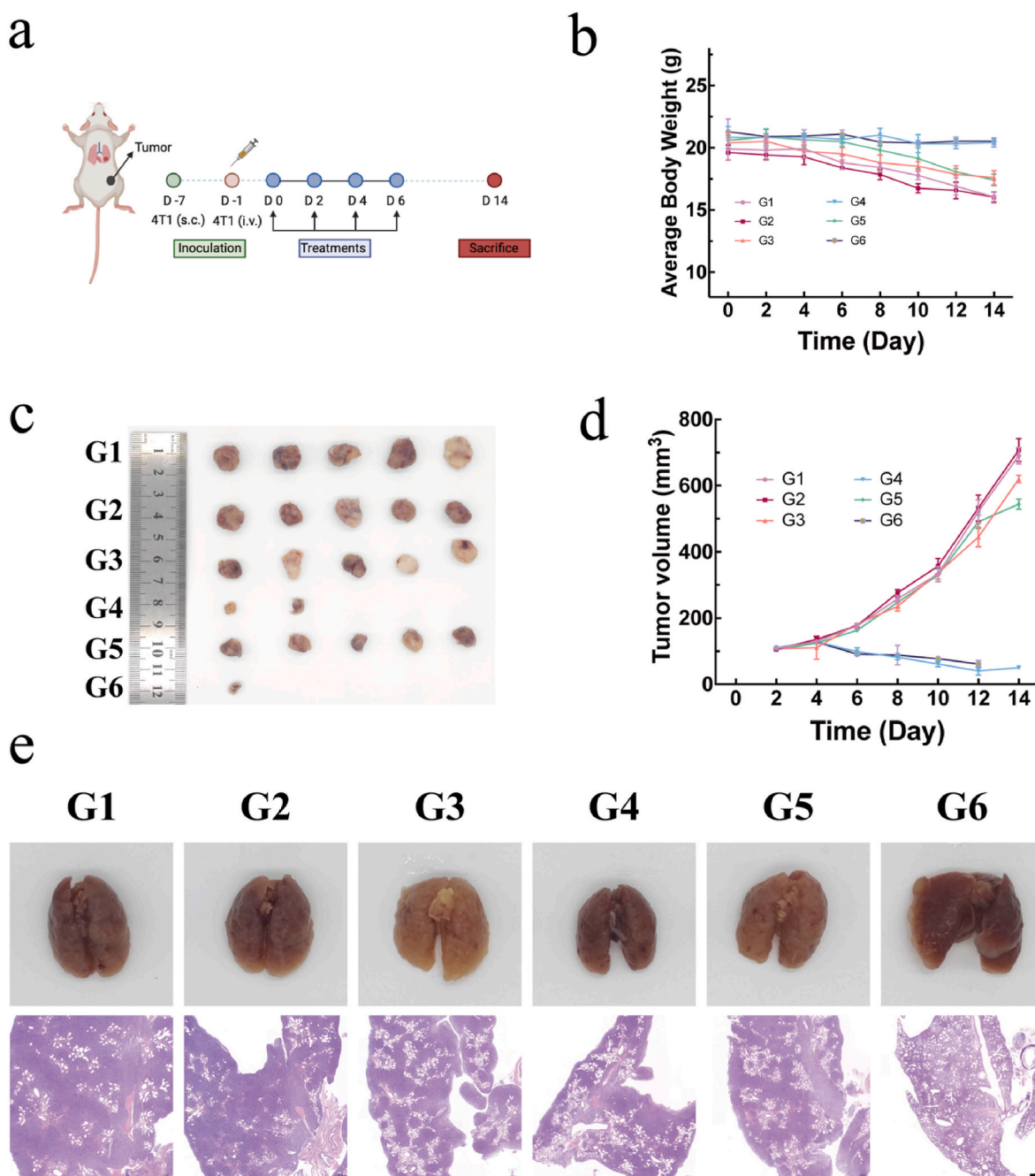
Fig. 5. a) Schematic illustration to evaluate the therapeutic efficacy and abscopal effect after treating with different formulations. b) Corresponding body weights of mice in each group after the mice are treated for 14 days. c) Photographs of tumours after treating with different formulations. d) tumour growth curves after treating with different formulations. e) The photographs and H&E-stained lung sections at day 14 after different treatments. Scale bar: 10 μm. G1: PBS; G2: PBS + L; G3: AuNCs@PDA; G4: AuNCs@PDA + L; G5: AuNCs@PDA-Mn; G6: AuNCs@PDA-Mn + L, in which the symbols "L", indicated the presence of NIR.

localised photothermal effects.

Following a series of treatments, the relative volume of tumours was recorded every two days. It was observed that the tumour volumes in the AuNCs@PDA and AuNCs@PDA-Mn groups were slightly smaller than those in the PBS group, indicating that relying solely on the CDT effect makes it difficult to effectively eliminate tumours. To enhance the tumour-killing ability, we incorporated PTT into the treatment formulas. In comparison to the PBS + L group, both AuNCs@PDA + L and AuNCs@PDA-Mn + L demonstrated a pronounced inhibition of tumour growth (Fig. 4e and g and S12). To ascertain whether these treatments would affect distant tumour growth in the absence of optical stimulation, the changes in the volume of distant tumours were evaluated. The

results demonstrated that NIR light stimulation significantly inhibited distant tumour growth and produced an abscopal effect on unirradiated tumours (Fig. 4f and I and S12). Furthermore, following the administration of various treatments, the survival rates of mice were monitored using a tumour volume endpoint criterion of 1500 mm^3. Furthermore, it is notable that the combined PTT/CDT exhibited a more pronounced survival advantage, compared with PTT or CDT alone (Fig. S13). Following a 14-day healing period, further confirmation of the synergistic therapeutic effects between hematoxylin and eosin (H&E), TdT-mediated dUTP Nick-End Labeling (TUNEL), and Ki67 staining demonstrated that AuNCs@PDA- Mn had the most prominent induction of cancer cell necrosis with the lowest apoptosis levels among all

treatments (Fig. 4h and j and S14). This further validates the superior inhibitory effects brought about by the introduction of NIR light stimulation.

The remarkable antitumour efficacy demonstrated by AuNCs@PDA and AuNCs@PDA-Mn prompted us to delve further into their efficacy in suppressing tumour metastasis. As displayed in Fig. 5a, the tumours were established on the flanks of the mice on days −7, and the lung metastasis model was established on days −1 by intravenous injection of free 4T1 cells, and the growth of tumour foci in the lungs of each group under different treatments were recorded at day 14. Due to the metastatic nature of the lung, mice in the other groups exhibited progressive weight loss at a later stage, accompanied by a significantly higher mortality rate compared to that observed in the AuNCs@PDA + L group and AuNCs@PDA-Mn + L group (Fig. 5b and S15). In contrast to the control group treated with PBS, the mice administered with AuNCs@PDA and AuNCs@PDA-Mn exhibited limited therapeutic results, primarily due to the suboptimal anticancer efficacy of AuNCs@PDA and AuNCs@PDA-Mn and the ineffective CDT. The antitumour efficacy of AuNCs@PDA + L and AuNCs@PDA-Mn + L was found to be relatively higher in mice (Fig. 5c and d and S16). Following the completion of the treatment regimen, lung tissues were collected and subjected to H&E staining in order to evaluate the efficacy of AuNCs@PDA-Mn + L in impeding the metastasis of 4T1 cancer cells (Fig. 5e). The results demonstrated that while AuNCs@PDA-Mn exhibited a modest inhibitory effect on metastatic tumours, combined irradiation yielded significantly enhanced anti-metastatic effects. This finding further substantiates the therapeutic potential of AuNCs@PDA-Mn + L in managing metastatic cancer.

3.6. In vivo immune response evaluation

In order to evaluate the antitumour immune efficacy and underlying mechanisms, the serum, tumour tissue, tumour-draining lymph nodes (TDLNs), and spleen samples were collected from mice on day 14 for immunological analysis. PTT, as a potent modality for tumour treatment, can effectively induce targeted and rapid cell death. The combination of CDT and PTT with AuNCs@PDA-Mn nanoparticles has the potential to enhance the efficacy of inducing tumour cell death and the release of DAMPs. Furthermore, the remnants of dead cells can act as TAAs, thereby activating the immune system. DCs, the primary antigen-presenting cell type, are capable of capturing and processing TAAs in nearby draining lymph nodes, while being activated by DAMPs to stimulate T-cell activation. During migration, dendritic cells modify TAAs, which are subsequently recognised by T-cell receptors. The process results in the upregulation of surface co-stimulatory molecules CD80 and CD86 on DCs, which is indicative of a mature phenotype [19–21]. In order to gain a deeper insight into the antitumour mechanisms of AuNCs@PDA-Mn-based PTT, we investigated its capacity to induce ICD in vivo. Here, CRT and HMGB1 were chosen as the characteristic indicators to examine their ability to induce ICD. As shown in Fig. S17, after irradiation, the exposure of CRT and the release of HMGB1 were significantly enhanced. The extent of DCs maturation is of critical importance in the successful activation of T cells. Mature DCs express all the essential stimulatory signals required for effective communication. Furthermore, activated T cells secrete pro-inflammatory cytokines, including IL-6, IL-12, IFN-γ and TNF-α, which contribute to immune-mediated tumour-killing effects. It is postulated that AuNCs@PDA-Mn + L may enhance the secretion of IFN-β by promoting the maturation of dendritic cells (DCs), subsequently guiding DCs to migrate from tumours to TDLNs and activating T cells. Consequently, we proceeded to collect TDLNs from mice at day 14 post-treatment, followed by subsequent flow cytometry analysis. The AuNCs@PDA-Mn group exhibited a moderate promotion of DC maturation (8.67 % ± 0.35 %) due to the presence of Mn^{2+}. However, in the AuNCs@PDA + L groups, an upregulation of CD11c expression on DCs (12.87 % ± 0.68 %) was observed, indicating a potential increase in

activated DCs (17.31 % ± 1.75 %) in the AuNCs@PDA-Mn + L group and suggesting enhanced efficiency in DC maturation (Figs. S18a and f). The quantification of $CD80^+$ $CD86^+$ DC cells and CD11c staining of lymph node tissues also indicated that a greater number of DCs matured in the AuNCs@PDA-Mn + L group (Figure S18b, c and g). Consequently, the secretion of immune-related cytokines, such as IFN-β and CXCL10, in both tumour tissue and serum exhibited a positive correlation with DC maturation (Figs. S18d and e; S19a and b). Furthermore, the remodelling of the TME was beneficial for the infiltration of $CD4^+$ T cells (Fig. 6a and S20a) and $CD8^+$ T cells (Fig. 6b–d and S20b-d) at the spleen regions of the mice in the AuNCs@PDA-Mn + L-treated group compared with the other groups, indicating a significant evocation of systemic immunity. Furthermore, the secretion of immune-related cytokines, including IL-6, IL-12, IFN-γ and TNF-α, was observed. As illustrated in Fig. 6e–h and S19c-f, the concentration of cytokines reached its highest level in the AuNCs@PDA-Mn + L group following treatment. This suggests that the combination of Mn^{2+} and PTT may induce strong immune responses. Furthermore, treatment with AuNCs@PDA-Mn + L effectively stimulates the activation of NK cells and plays a pivotal role in enhancing the antibody-mediated immune response against tumours (Fig. 6i and S21).

3.7. Assessment of biosafety of AuNCs@PDA and AuNCs@PDA-Mn

The biocompatibility of nanoparticles is of paramount importance for their biomedical applications. In this study, the biocompatibility of AuNCs@PDA and AuNCs@PDA-Mn was evaluated in a healthy Balb/C mouse model using the same treatment formulas. The results of the therapeutic experiment demonstrated that both AuNCs@PDA and AuNCs@PDA-Mn did not exhibit significant acute toxicity in mice. Furthermore, the biocompatibility of AuNCs@PDA and AuNCs@PDA-Mn was evaluated by measuring organ biomarkers in serum, including aspartate transaminase (AST), alanine transaminase (ALT), alkaline phosphatase (ALP), uric acid (UA), creatinine (CR), creatine kinase (CK), creatine kinase MB isoenzyme (CKMB) and lactate dehydrogenase (LDH). Ultimately, the results of the blood biochemical analysis demonstrated that there were no significant changes in the levels of organ biomarkers on day 14 following the administration of the final injection (Fig. S22). Furthermore, analysis of mouse blood routine indexes and major organ tissue staining with H&E demonstrated that intravenous injection of both AuNCs@PDA and AuNCs@PDA-Mn did not induce abnormal blood cell counts or cause unnecessary damage to major organs (Fig. S23). In conclusion, these findings indicate that at the tested doses, both AuNCs@PDA and AuNCs@PDA-Mn possess excellent biocompatibility.

4. Conclusion

In summary, a metal-phenolic network coated AuNCs was designed and synthesised by a green approach for cancer therapy. On the one hand, AuNCs@PDA-Mn exhibits excellent photothermal conversion efficiency, effectively suppressing tumour growth after 10 min of irradiation at the tumour site using an 808 nm laser (1.0 W/cm²). On the other hand, Mn-induced Fenton-like reaction significantly enhances the hypoxic microenvironment within tumours, depleting GSH and further impeding tumour progression. Moreover, thermotherapy-induced immunogenic cell death promotes DCs maturation and activates cytotoxic $CD8^+$ T cells, helper $CD4^+$ T cells, as well as NK cells. Combined with a plethora of hyperthermia- and ROS-mediated double-hit damage to tumour-associated antigens (TAAs), this synergistically augments both innate and adaptive anti-tumour immunity while achieving localised hyperthermic/enhanced immune treatment effects that can trigger systemic immune responses. Based on the compositional simplicity of Mn^{2+} and the activation characteristics of cGAS-STING, we have developed a biocompatible nano photosensitiser rich in manganese (AuNCs@PDA-Mn), which enables efficient immunotherapy and enhanced photothermal therapy. This innovative approach has the
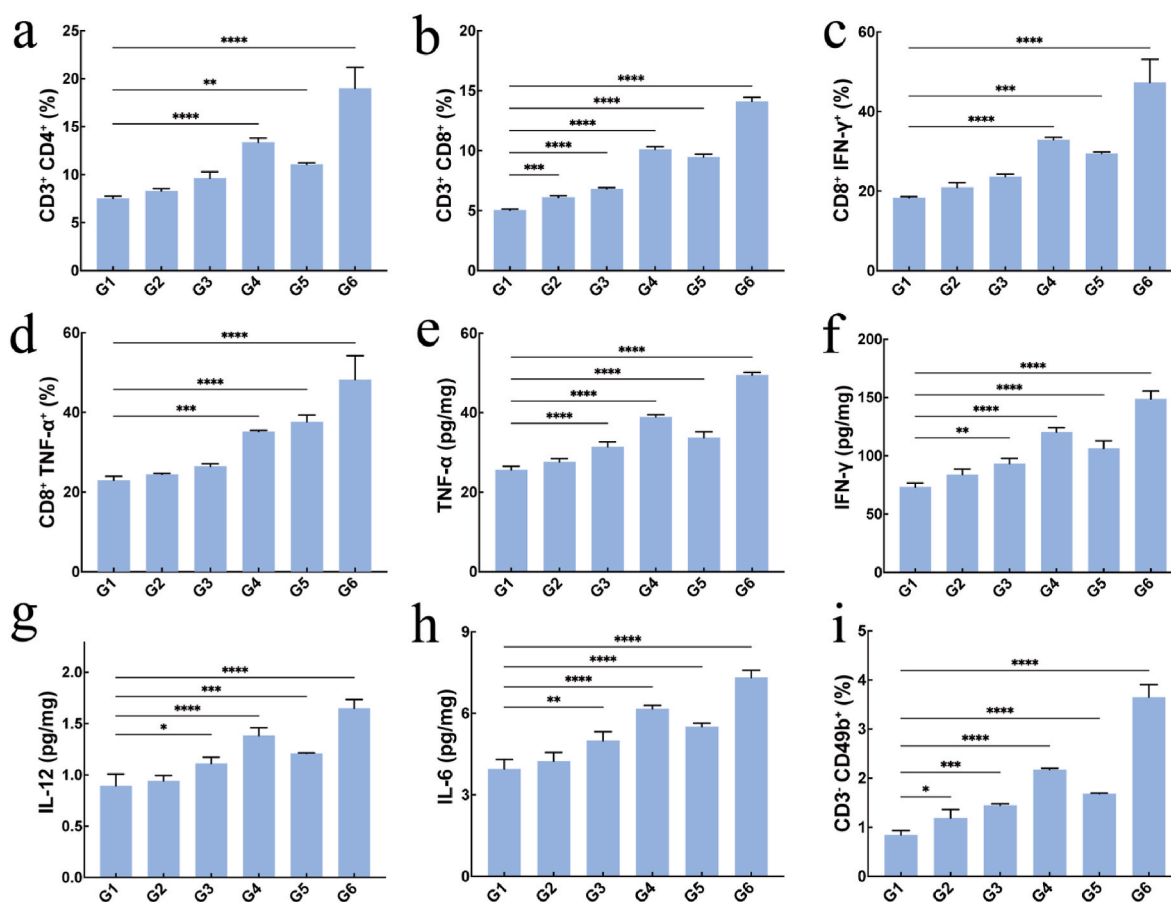
Fig. 6. a-d) The quantification of CD3$^+$ CD4$^+$, CD3$^+$ CD8$^+$, CD8$^+$ IFN-γ$^+$, CD8$^+$ TNF-α$^+$ T cells. e-g) TNF-α, IFN-γ, IL-12 and IL-6 secretion in tumour tissues. i) The quantification of CD49b$^+$ CD3$^-$ NK cells. Data are presented as mean ± SD (n = 3). G1: PBS; G2: PBS + L; G3: AuNCs@PDA; G4: AuNCs@PDA + L; G5: AuNCs@PDA-Mn; G6: AuNCs@PDA-Mn + L, in which the symbols "L", indicated the presence of NIR irradiation. Statistical significance was calculated via one-way ANOVA with Tukey's test: *p < 0.05; **p < 0.01; ***p < 0.001; ****p < 0.0001.

potential to revolutionise the field of cancer treatment and should be subjected to further comprehensive investigation.

CRediT authorship contribution statement

Tingyu Yang: Writing – original draft, Validation, Software, Methodology, Investigation, Data curation, Conceptualization. **Liqun Dai:** Methodology, Investigation, Conceptualization. **Jie Liu:** Methodology, Investigation. **Yi Lu:** Investigation. **Meng Pan:** Methodology, Investigation. **Lili Pan:** Methodology. **Lin Ye:** Investigation. **Liping Yuan:** Investigation. **Xicheng Li:** Investigation. **Zhongwu Bei:** Investigation. **Zhiyong Qian:** Writing – review & editing, Supervision, Funding acquisition, Conceptualization.

Ethics approval and consent to participate

All animal experiments were performed following the protocols approved by the Ethics Committee of the Animal Experimental Center of State Key Laboratory of Biotherapy of Sichuan University (Checking number: 20210409028), and were carried out in compliance with all relevant ethical regulations.

Declaration of competing interest

Zhiyong Qian is an editorial board member for Bioactive Materials and was not involved in the editorial review or the decision to publish this article. The authors declare that they have no known competing financial interests or personal relationships that could have appeared to influence the work reported in this paper.

Appendix A. Supplementary data

Supplementary data to this article can be found online at https://doi.org/10.1016/j.bioactmat.2024.10.021.

References

[1] F. Bray, M. Laversanne, H. Sung, J. Ferlay, R.L. Siegel, I. Soerjomataram, A. Jemal, Global cancer statistics 2022: GLOBOCAN estimates of incidence and mortality worldwide for 36 cancers in 185 countries, Ca-Cancer J. Clin. 74 (3) (2024) 229–263.

[2] S.Y. Lei, R.S. Zheng, S.W. Zhang, S.M. Wang, R. Chen, K.X. Sun, H.M. Zeng, J. C. Zhou, W.Q. Wei, Global patterns of breast cancer incidence and mortality: a population-based cancer registry data analysis from 2000 to 2020, Cancer Commun. 41 (11) (2021) 1183–1194.

[3] W.F. Anderson, P.S. Rosenberg, A. Prat, C.M. Perou, M.E. Sherman, How many etiological subtypes of breast cancer: two, three, four, or more? Jnci-Journal of the National Cancer Institute 106 (8) (2014).

[4] G. Bianchini, J.M. Balko, I.A. Mayer, M.E. Sanders, L. Gianni, Triple-negative breast cancer: challenges and opportunities of a heterogeneous disease, Nat. Rev. Clin. Oncol. 13 (11) (2016) 674–690.

[5] L. Yin, J.-J. Duan, X.-W. Bian, S.-c. Yu, Triple-negative breast cancer molecular subtyping and treatment progress, Breast Cancer Res. 22 (1) (2020).

[6] L.N. Chaudhary, K.H. Wilkinson, A. Kong, Triple-negative breast cancer who should receive neoadjuvant chemotherapy? Surg. Oncol. Clin. 27 (1) (2018), 141-+.

[7] Y. Li, H.J. Zhang, Y. Merkher, L. Chen, N. Liu, S. Leonov, Y.H. Chen, Recent advances in therapeutic strategies for triple-negative breast cancer, J. Hematol. Oncol. 15 (1) (2022).

[8] S.Y. Hwang, S. Park, Y. Kwon, Recent therapeutic trends and promising targets in triple negative breast cancer, Pharmacology & Therapeutics 199 (2019) 30–57.

[9] E.C. Dreaden, M.A. Mackey, X.H. Huang, B. Kang, M.A. El-Sayed, Beating cancer in multiple ways using nanogold, Chem. Soc. Rev. 40 (7) (2011) 3391–3404.

[10] X. Zhu, W. Feng, J. Chang, Y.-W. Tan, J. Li, M. Chen, Y. Sun, F. Li, Temperature-feedback upconversion nanocomposite for accurate photothermal therapy at facile temperature, Nat. Commun. 7 (2016).

[11] H. Deng, J. Zhang, Y. Yang, J. Yang, Y. Wei, S. Ma, Q. Shen, Chemodynamic and photothermal combination therapy based on dual-modified metal-organic framework for inducing tumor ferroptosis/pyroptosis, Acs Applied Materials & Interfaces 14 (21) (2022) 24089–24101.

[12] S. Wang, Y. Pang, S. Hu, J. Lv, Y. Lin, M. Li, Copper sulfide engineered covalent organic frameworks for pH-responsive chemo/photothermal/chemodynamic synergistic therapy against cancer, Chem. Eng. J. 451 (2023).

[13] P. Manivasagan, A. Joe, H.-W. Han, T. Thambi, M. Selvaraj, K. Chidambaram, J. Kim, E.-S. Jang, Recent advances in multifunctional nanomaterials for photothermal-enhanced Fenton-based chemodynamic tumor therapy, Materials Today Bio 13 (2022).

[14] W. Li, J. Yang, L. Luo, M. Jiang, B. Qin, H. Yin, C. Zhu, X. Yuan, J. Zhang, Z. Luo, Y. Du, Q. Li, Y. Lou, Y. Qiu, I. You, Targeting photodynamic and photothermal therapy to the endoplasmic reticulum enhances immunogenic cancer cell death, Nat. Commun. 10 (2019).

[15] Z. Yang, D. Gao, X. Guo, L. Jin, J. Zheng, Y. Wang, S. Chen, X. Zheng, L. Zeng, M. Guo, X. Zhang, Z. Tian, Fighting immune cold and reprogramming immunosuppressive tumor microenvironment with red blood cell membrane-camouflaged nanobullets, ACS Nano 14 (12) (2020) 17442–17457.

[16] Z. Li, X. Lai, S. Fu, L. Ren, H. Cai, H. Zhang, Z. Gu, X. Ma, K. Luo, Immunogenic cell death activates the tumor immune microenvironment to boost the immunotherapy efficiency, Adv. Sci. 9 (22) (2022).

[17] D. Zhang, J. Zhang, Q. Li, A. Song, Z. Li, Y. Luan, Cold to hot: rational design of a minimalist multifunctional photo-immunotherapy nanoplatform toward boosting immunotherapy capability, Acs Applied Materials & Interfaces 11 (36) (2019) 32633–32646.

[18] X. Zhang, J. Tang, C. Li, Y. Lu, L. Cheng, J. Liu, A targeting black phosphorus nanoparticle based immune cells nano-regulator for photodynamic/photothermal and photo-immunotherapy, Bioact. Mater. 6 (2) (2021) 472–489.

[19] J. Nam, S. Son, L.J. Ochyl, R. Kuai, A. Schwendeman, J.J. Moon, Chemo-photothermal therapy combination elicits anti-tumor immunity against advanced metastatic cancer, Nat. Commun. 9 (2018).

[20] J.Y. Zhou, G.Y. Wang, Y.Z. Chen, H.X. Wang, Y.Q. Hua, Z.D. Cai, Immunogenic cell death in cancer therapy: present and emerging inducers, J. Cell Mol. Med. 23 (8) (2019) 4854–4865.

[21] M.Q. Zhu, M.D. Yang, J.J. Zhang, Y.Z. Yin, X. Fan, Y. Zhang, S.S. Qin, H. Zhang, F. Yu, Immunogenic cell death induction by ionizing radiation, Front. Immunol. 12 (2021).

[22] X. Dai, X. Zhao, Y. Liu, B. Chen, X. Ding, N. Zhao, F.-J. Xu, Controlled synthesis and surface engineering of janus chitosan-gold nanoparticles for photoacoustic imaging-guided synergistic gene/photothermal therapy, Small 17 (11) (2021).

[23] Y. Zheng, J. Wu, H. Jiang, X. Wang, Gold nanoclusters for theranostic applications, Coord. Chem. Rev. 431 (2021).

[24] B. Zhang, J. Chen, Y. Cao, O.J.H. Chai, J. Xie, Ligand design in ligand-protected gold nanoclusters, Small 17 (27) (2021).

[25] M. Guo, G. Zhang, R. Zhao, H. Ma, Y. Yan, S. Yang, J. Meng, Y. Huang, X.-D. Zhang, H. Wang, R. Zhang, Ligand engineering of gold nanoclusters for NIR-II imaging, ACS Appl. Nano Mater. 6 (17) (2023) 15945–15958.

[26] Y.G. Srinivasulu, Q. Yao, N. Goswami, J. Xie, Interfacial engineering of gold nanoclusters for biomedical applications, Mater. Horiz. 7 (10) (2020) 2596–2618.

[27] F. Xiao, Y. Chen, J. Qi, Q. Yao, J. Xie, X. Jiang, Multi-targeted peptide-modified gold nanoclusters for treating solid tumors in the liver, Adv. Mater. 35 (20) (2023).

[28] S. Li, N.-N. Li, X.-Y. Dong, S.-Q. Zang, T.C.W. Mak, Chemical flexibility of atomically precise metal clusters, Chem. Rev. 124 (11) (2024) 7262–7378.

[29] N. Yang, Y. Kang, Y. Cong, X. Wang, C. Yao, S. Wang, L. Li, Controllable gold nanocluster-emulsion interface for direct cell penetration and photothermal killing, Adv. Mater. 35 (50) (2023).

[30] C.Y. Jia, Y.X. Guo, F.G. Wu, Chemodynamic therapy via Fenton and fenton-like nanomaterials: strategies and recent advances, Small 18 (6) (2022).

[31] Z.M. Tang, Y.Y. Liu, M.Y. He, W.B. Bu, Chemodynamic therapy: tumour microenvironment-mediated Fenton and fenton-like reactions, Angewandte Chemie-International Edition 58 (4) (2019) 946–956.

[32] Z. Tang, H. Zhang, Y. Liu, D. Ni, H. Zhang, J. Zhang, Z. Yao, M. He, J. Shi, W. Bu, Antiferromagnetic pyrite as the tumor microenvironment-mediated nanoplatform for self-enhanced tumor imaging and therapy, Adv. Mater. 29 (47) (2017).

[33] Y. Liu, W. Zhen, L. Jin, S. Zhang, G. Sun, T. Zhang, X. Xu, S. Song, Y. Wang, J. Liu, H. Zhang, All-in-One theranostic nanoagent with enhanced reactive oxygen species generation and modulating tumor microenvironment ability for effective tumor eradication, ACS Nano 12 (5) (2018) 4886–4893.

[34] M. Wang, M. Chang, Q. Chen, D. Wang, C. Li, Z. Hou, J. Lin, D. Jin, B. Xing, Au2Pt-PEG-Ce6 nanoformulation with dual nanozyme activities for synergistic chemodynamic therapy/phototherapy, Biomaterials 252 (2020).

[35] X. Guo, N. Yang, W. Ji, H. Zhang, X. Dong, Z. Zhou, L. Li, H.-M. Shen, S.Q. Yao, W. Huang, Mito-bomb: targeting mitochondria for cancer therapy, Adv. Mater. 33 (43) (2021).

[36] S. Sun, Q. Chen, Z. Tang, C. Liu, Z. Li, A. Wu, H. Lin, Tumor microenvironment stimuli-responsive fluorescence imaging and synergistic cancer therapy by carbon-dot-Cu²⁺Nanoassemblies, Angewandte Chemie-International Edition 59 (47) (2020) 21041–21048.

[37] M. Zhan, F. Wang, Y. Liu, J. Zhou, W. Zhao, L. Lu, J. Li, X. He, Dual-cascade activatable nanopotentiators reshaping adenosine metabolism for sono-chemodynamic-immunotherapy of deep tumors, Adv. Sci. 10 (10) (2023).

[38] L.-H. Fu, Y.-R. Hu, C. Qi, T. He, S. Jiang, C. Jiang, J. He, J. Qu, J. Lin, P. Huang, Biodegradable manganese-doped calcium phosphate nanotheranostics for traceable cascade reaction-enhanced anti-tumor therapy, ACS Nano 13 (12) (2019) 13985–13994.

[39] T. Xiao, M. He, F. Xu, Y. Fan, B. Jia, M. Shen, H. Wang, X. Shi, Macrophage membrane-camouflaged responsive polymer nanogels enable magnetic resonance imaging-guided chemotherapy/chemodynamic therapy of orthotopic glioma, ACS Nano 15 (12) (2021) 20377–20390.

[40] Y. Zheng, J. Chen, X.R. Song, M.Q. Chang, W. Feng, H. Huang, C.X. Jia, L. Ding, Y. Chen, R. Wu, Manganese-enriched photonic/catalytic nanomedicine augments synergistic anti-TNBC photothermal/nanocatalytic/immuno-therapy via activating cGAS-STING pathway, Biomaterials 293 (2023).

[41] B. Li, Z. Wu, X. Xu, Y. Lv, Y. Guo, S. Liang, Z. Wang, L. He, Y.-F. Song, GSH/pH dual-activated POM@MOF for tumor cell-specific synergistic photothermal and chemodynamic therapy, Inorg. Chem. Front. 11 (14) (2024) 4439–4448.

[42] S. Du, Y. Luo, Z. Liao, W. Zhang, X. Li, T. Liang, F. Zuo, K. Ding, New insights into the formation mechanism of gold nanoparticles using dopamine as a reducing agent, J. Colloid Interface Sci. 523 (2018) 27–34.

[43] Q. Ye, F. Zhou, W. Liu, Bioinspired catecholic chemistry for surface modification, Chem. Soc. Rev. 40 (7) (2011) 4244–4258.

[44] W. Cheng, X. Zeng, H. Chen, Z. Li, W. Zeng, L. Mei, Y. Zhao, Versatile polydopamine platforms: synthesis and promising applications for surface modification and advanced nanomedicine, ACS Nano 13 (8) (2019) 8537–8565.